Biosensors and Bioelectronics 278 (2025) 117349

Contents lists available at ScienceDirect

Biosensors and Bioelectronics

journal homepage: www.elsevier.com/locate/bios

Evaporative cooling for low-cost monitoring of flow of cerebrospinal fluid through shunts in patients with hydrocephalus

Minsu Park [a,1], Shupeng Li [b,1], Kyeong Min Song [c], Kyeongha Kwon [d], Jung-Ho Yun [e], Raudel Avila [f], R. Chad Webb [g], Hany M. Arafa [c], Soongwon Cho [c], Geumbee Lee [h], Chase Correira [g], Bosung Kim [c], Yu Bin Kim [i], Hyoun Ji Ha [i], Woo-Youl Maeng [c], Jae-Young Yoo [j], Hyoyoung Jeong [k], Hanjun Ryu [l], Sang Min Won [m], Yei Hwan Jung [n], Yoonseok Park [o,p], Seong Jun Kang [i], Yonggang Huang [b,**], John A. Rogers [b,g,q,r,s,*]

[a] Department of Polymer Science and Engineering, Dankook University, Yongin, 16890, Republic of Korea
[b] Department of Mechanical Engineering, Northwestern University, Evanston, IL, 60208, USA
[c] Querrey Simpson Institute for Bioelectronics, Northwestern University, Evanston, IL, 60208, USA
[d] School of Electrical Engineering, Korea Advanced Institute of Science and Technology, Daejeon, 34141, Republic of Korea
[e] Department of Neurosurgery, Trauma Center, Dankook University Hospital, Cheonan, 31116, Republic of Korea
[f] Department of Mechanical Engineering, Rice University, Houston, TX, 77005, USA
[g] Rhaeos Inc., Evanston, IL, 60201, USA
[h] Department of Chemical Engineering, Kyungpook National University, Daegu, 41566, Republic of Korea
[i] Department of Advanced Materials Engineering for Information and Electronics, Kyung Hee University, Yongin, 17104, Republic of Korea
[j] Department of Semiconductor Convergence Engineering, Sungkyunkwan University, Suwon, 16419, Republic of Korea
[k] Department of Electrical and Computer Engineering, University of California, Davis, CA, 95616, USA
[l] Department of Advanced Materials Engineering, Chung-Ang University, Anseong, 17546, Republic of Korea
[m] Department of Electrical and Computer Engineering, Sungkyunkwan University, Suwon, 16419, Republic of Korea
[n] Department of Electronic Engineering, Hanyang University, Seoul, 04763, Republic of Korea
[o] Department of Advanced Materials Engineering for Information and Electronics, Integrated Education Institute for Frontier Science & Technology (BK21 Four), Kyung Hee University, Yongin, 17104, Republic of Korea
[p] KHU-KIST Department of Converging Science and Technology, Kyung Hee University, Seoul, 02447, Republic of Korea
[q] Department of Materials Science and Engineering, Northwestern University, Evanston, IL, 60208, USA
[r] Department of Biomedical Engineering, Northwestern University, Evanston, IL, 60208, USA
[s] Department of Neurological Surgery, Feinberg School of Medicine, Northwestern University, Chicago, IL, 60611, USA

ARTICLE INFO

Keywords:
Bioelectronics
Hydrocephalus
Flow sensor
Passive cooling
Thermochromic liquid crystal

ABSTRACT

Hydrocephalus, a neurological disorder caused by an abnormal accumulation of cerebrospinal fluid (CSF) in the brain, manifests in symptoms such as headaches, blurred vision, and balance issues. While ventriculoperitoneal shunting is a common treatment, it has high failure rates, especially in pediatric patients. Recent progress in continuous, non-invasive monitoring using skin-mounted sensors based on anemometric techniques and transient plane source methods offer significant promise. Here, we introduce an advanced device of this general type, configured for ultralow power operation and cost-effective construction. The innovation involves replacing heating elements with passive cooling mechanisms driven by water evaporation, thereby reducing the need for high-capacity battery power. Localized cooling at the shunt position (ΔT_{skin} ~6 °C) enables flow measurements by creating differential temperature changes in upstream and downstream regions. Quantitative models of thermal transport and systematic experimental studies enable optimized design choices. A compact device with Bluetooth Low Energy (BLE) capabilities and a small battery allows both intermittent evaluations and continuous monitoring. Additional measurements confirm capabilities in accurate flow measurements using passive, non-

* Corresponding author. Department of Mechanical Engineering, Northwestern University, Evanston, IL, 60208, USA.
** Corresponding author.
E-mail addresses: y-huang@northwestern.edu (Y. Huang), jrogers@northwestern.edu (J.A. Rogers).
[1] M.P.,S.L. contributed equally to this work.

https://doi.org/10.1016/j.bios.2025.117349
Received 24 September 2024; Received in revised form 1 March 2025; Accepted 5 March 2025
Available online 16 March 2025

electronic skin patches, where readout occurs based on colorimetric evaluations of thermochromic liquid crystal (TLC) arrays by digital image analysis. These results provide versatile, cost-effective, and accessible shunt monitoring options suitable for use even in the most resource-constrained regions of lower- and middle-income countries.

1. Introduction

Hydrocephalus is a neurological disorder characterized by an abnormal accumulation of cerebrospinal fluid (CSF) within the ventricles of the brain. This condition occurs when CSF is excessively produced or not adequately drained, leading to non-specific symptoms such as headache, blurred vision, nausea and balance problems (Kahle et al., 2016). In 2019, there were 36,898 shunt-related hospital admissions, accounting for 495,138 hospital days and a total cost of more than $2.06 billion (Koschnitzky et al., 2023). A widely recommended treatment for hydrocephalus involves the surgical insertion of a ventriculoperitoneal (VP) shunt. The VP shunt resides in the intracranial space and connects to a flexible tube that passes under the skin to allow excess CSF to drain to the chest cavity or abdomen, where it absorbs into the body. Although highly effective, such shunts suffer from high rates of failure, at levels of up to 50% in pediatric populations over six years (Liptak et al., 1985; McGirt et al., 2002). More than 28% of shunt recipients require at least one revision surgery within the first year after implantation (Al-Tamimi et al., 2014; Kestle et al., 2000).

Methods for continuous and reliable measurements of CSF flow through shunts are therefore of interest to enable early detection of a malfunction. Recent approaches can be classified into two categories: i) sensors that integrate directly into the shunt catheter and ii) external evaluations based on medical imaging techniques available in hospital settings. Approaches in the first category rely on components that exploit electrostatic or thermal mechanisms to assess flow directly (Bork et al., 2010; Kim et al., 2016; Zarrin et al., 2023) in a continuous fashion that facilitates early detection of problems without the need for hospital visits. The first example incorporates a complementary metal-oxide-semiconductor (CMOS) flow sensor based on the thermal anemometer principle, directly integrating it with the shunt. This sensor embeds within a packaged transducer comprising RF electronics, an antenna, and a microcontroller for passive telemetry (Bork et al., 2010). The second example employs in-line capacitive measurements to assess the patency of a drainage port by monitoring impedance changes between electrodes positioned on the internal and external surfaces of the shunt. Disturbances in this impedance indicate blockages in the ionic conductive path. Increases in obstruction reduce the cross-sectional area available for conduction, resulting in a corresponding increase in impedance (Kim et al., 2016). A more recent study presents a sensor that integrates metal electrodes into an existing shunt. By applying a pulsed voltage, this sensor generates charged ion clouds within the CSF flow, enabling detection of a potential difference between the upstream emitter and the downstream detector plates (Zarrin et al., 2023). A key disadvantage with each of these examples is in the requirement for implantable electronics and wireless communication hardware, with associated potential for complications or device failures. Examples of the second category include magnetic resonance imaging (MRI) and computed tomography (CT) scans to assess changes in ventricle size which may occur due to blockages of flow (Linninger et al., 2007), as well as phase-contrast MRI (PC-MRI) to assess fluid dynamics through the shunt (Ha et al., 2023). Complementary methods include X-ray imaging to identify breaks, disconnections, or kinks in the shunt catheter (Vassilyadi et al., 2010). Specialized techniques such as radionuclide shuntography rely on injection of radioactive material into the shunt and tracking its movement with a gamma camera (Gok et al., 2013). Although these methods now represent established clinical protocols, they provide only intermittent assessments of shunt function, they require hospital visits, they expose patients to ionizing radiation with repeated imaging, and they are costly and time-consuming.

A recent alternative approach involves passive or active skin-mounted devices for thermal actuation and temperature sensing, with successful demonstrations of accurate CSF flow measurements in both benchtop and clinical settings (Chiba and Yuda, 1980; Madsen et al., 2011). In particular, fully integrated, soft devices that mount on the skin for continuous measurements of flow using thermal techniques are attractive. The most versatile platforms combine use of a transient plane source (TPS) method (Gustafsson, 1991; Madhvapathy et al., 2022) with spatial mapping of temperature distribution local to the plane source (Krishnan et al., 2020; Webb et al., 2015), where flow creates anisotropy in the temperature distribution that results from a mild temperature increase at a localized position along the length of the shunt. Specifically, the sensing scheme employs a central heater positioned between two temperature sensors (upstream and downstream), all mounted on the skin at a location above and aligned with the shunt. Thermal transport, which occurs through the skin, the shunt and the CSF, results in a temperature difference between the upstream and downstream sensors (ΔT_{UD}). Theoretical models that connect ΔT_{UD} to the flow rate serve as the basis for precisely evaluating not only the presence or absence of flow, but also the volumetric rate of flow. An integrated device includes these thermal elements along with a wireless module for two-way communication with a portable device such as a smartphone. Comprehensive analytical models of heat transport, validating benchtop experiments and human clinical studies establish a strong engineering foundation (Krishnan et al., 2018, 2020). With this approach, the heater must, however, deliver a constant heat flux ($\sim$3.3 mW mm^{-2}) to the skin to generate a robust and easily quantified difference in temperature, typically in the range of $\Delta T_{UD} > \sim$0.5 K for real-world applications (Krishnan et al., 2020). This requirement largely determines the operational lifetime, set by the capacity of the battery. Another drawback is that the maximum temperature increase that the skin can tolerate—typically below 10 K for short time durations—places a limit on measurement sensitivity.

Here, we present an advanced version of this type of device platform, designed to enable continuous, low-cost, wireless measurement of CSF flow, with a particular emphasis on the use of a passive cooler as a thermal actuator. In particular, the device incorporates a cooling foam that functions through water evaporation, thereby eliminating the need for a heater and its associated power consumption. Localized cooling (ΔT_{skin} $\sim$6 °C, T_{skin}: temperature of the skin) of the skin surface at the shunt position serves as the basis for flow measurements by inducing differential changes in temperature in the upstream and downstream regions. Theoretical and numerical models of thermal transport and system-level mechanics simulations guide the optimization of both materials selections and design layouts. On-skin measurements with a compact device that also incorporates a Bluetooth Low Energy (BLE) system on a chip (SoC) and small battery validate its operation as a realistic option for both short "spot-checks" and for measuring variations in flow rate under indoor conditions on hydrocephalus patients. Furthermore, we demonstrate a colorimetric flow sensing scheme that further minimizes energy consumption, device cost and design complexity by replacing the BLE electronics for wireless data transfer with an imaging scheme that relies on the digital camera function in standard smartphones. Benchtop studies indicate feasibility for accurate flow measurements using a passive, non-electronic skin patch that integrates thermochromic liquid crystal (TLC) dot arrays and evaporative cooling mechanisms. These collective results provide versatile options for shunt monitoring across patients of various ages, with features in

cost, simplicity and deployability that suggest feasibility for use in even the most resource-constrained regions of lower- and middle-income countries.

2. Methods

2.1. Performing benchtop experiments

The phantom shunt assembly consists of a three-dimensional (3D)-printed mold that incorporates a medical grade, distal catheter (1.3 mm inner diameter (ID)/2.5 mm outer diameter (OD), Medtronic). A matrix of polydimethylsiloxane (PDMS) (Sylgard 170, Dow Corning) serves as a skin phantom. Casting PDMS onto a mold with defined heights yielded different skin depths (h_{skin}). Immersing the skin phantom in a water bath with temperature controlled by a proportional-integral-differential (PID) controller of a hot plate stably regulated the surface temperature of the skin phantom to a desired value. A calibrated syringe pump (Harvard Apparatus) enabled programmed control of flow rates. Measurement and visualization of thermal distributions relied on an infrared (IR) camera (FLIR Systems, a6255sc). An isolated cooler or an electronic device with a cooler were mounted on the top surface of the skin phantom in such a manner that the center of the cooler aligned with the flow passage.

2.2. Fabricating the electronics

Eagle CAD version 9.6.2 (Autodesk) served as the basis for generating schematics and layouts for the flexible printed circuit board (fPCB). The fPCB consists of a layer of polyimide (PI; 25 μm thick) with patterned copper traces (Cu; 18 μm thick) on the top and bottom surfaces, each encapsulated with a layer of insulating PI (12.5 μm thick) bonded with a silicon adhesive (12 μm thick). An International Organization for Standardization (ISO) 9001-compliant PCB manufacturer produced fPCB. Various surface-mounted components, including Bluetooth Low Energy (BLE) system-on-a-chip (BLE-SoC; nRF52832, Nordic Semiconductor), antenna (2450AT18A100, Johanson Technology), negative temperature coefficient (NTC) thermistor (NCP03XH, Murata), and passive components (resistors, capacitors, and inductors) were bonded onto the fPCB with a low temperature reflow soldering process using solder paste (TS391LT, Chip Quik) and a soldering heat gun (AOYUE Int866). A BLE-SoC with configured analog front-end circuits transmitted the responses of the NTC thermistors to a BLE-enabled smartphone. This process allowed for real-time graphical display and storage of the time-dependent differences in temperature between the thermistor at upstream (TH_{US}) and the thermistor at downstream (TH_{DS}) sensor locations. The electrical power was determined by calculating the product of current (I) and voltage (V) using formula $P = I \times V$. A Power Profiler Kit II (PPK2) board (nRF-PPK2, Nordic Semiconductor) measured the current of the device. The PPK2 supplied power to the device and its Analog-to-Digital Converter (ADC) captured the voltage drop across a series measurement resistor. The current consumed by the device is expressed as I = measured voltage drop (V)/resistor value (Ω). The PPK board was connected to a computer via an nRF9160 development kit board (nRF9160 DK, Nordic Semiconductor), and the PPK application provided a real-time display of the current measurements. These results enabled estimates of the battery life of the device.

2.3. Encapsulating the electronics

The top and bottom encapsulation layers were crafted from a soft silicone-based material (Silbione RTV4420, Elkem) through molding and curing at 80 °C. The top and bottom aluminum molds were formed using a three-axis milling machine (Modela Pro II MDX 540, Roland DGA). The encapsulation procedure involved placing the bottom encapsulation layer on the bottom aluminum mold, mounting the fPCB with electronic components along with the cooler on this layer, then covering it with the top encapsulation layer and bonding the assembly with uncured silicone elastomer. After curing overnight at room temperature, a custom die tool (MillenniumDie) cut away the excess encapsulation layers, completing the fabrication process.

2.4. Finite element analysis (FEA) simulations for bending mechanics

The mechanical compliance of the device was modeled using the commercial finite element software ABAQUS (Analysis User's Manual, 2023) to quantify the strain levels in both the device and the electronic layers during bending deformations, such as those experienced when the device is placed on the neck of a child or adult for continuous flow monitoring. The simulation results of the strain distribution in the electronic layers indicate that the device can seamlessly deform to a radius of curvature of 58 mm (bending angle 21.8°) for an adult neck and 42 mm (bending angle 30.1°) for a child's neck. Additionally, the strain in the metal layer remains below the yield strain (0.3%), ensuring elastic deformation during placement. The highest strain (~0.17%) is concentrated on the electronic traces connecting to the thermistors near the evaporative cooler. Because the electronics are strategically placed near the neutral mechanical plane of deformation, this strain value remains below the yield strain for both neck curvatures. Hexahedron elements (C3D8R) mesh the silicone encapsulation layer while shell elements (S4R) mesh the thin fPCB and electronic layers (50 μm) in the model. The total number of elements in the simulations is ~875,000. The minimal element size was 1/8th the width the copper traces (200 μm), which ensured convergence of the mesh, and accuracy of the simulation results. The elastic modulus (E) and Poisson's ratio (ν) used in the analysis were $E_{copper} = 119$ GPa, $\nu_{copper} = 0.34$ for the copper traces, $E_{silicone} = 130$ kPa, $\nu_{silicone} = 0.49$ for the silicone encapsulation, $E_{fPCB} = 2.5$ GPa, $\nu_{fPCB} = 0.4$ for the fPCB, and $E_{foam} = 2$ MPa, $\nu_{foam} = 0.3$ for the evaporative cooling foam.

2.5. Finite element analysis (FEA) simulations for characterizing thermal flow

The commercial software Ansys Fluent was used to study the thermal response of the cooling-based flow sensing system. The same 3D model as Fig. S9 was built with $h_{skin} = 0.5$ mm. Hexahedron elements were applied to the fluid part and tetrahedral elements were applied to all the solid parts, elements was refined to the fluid and catheter parts to ensure computational accuracy. A constant surrounding temperature (33 °C) around the side and bottom walls in the 3D model was imposed to account the effect of the water bath and a constant cooling power of 210 kW m^{-3} was fitted by the temperature of the cooler (T_{cooler}) without flow (26 °C) to account for the evaporative cooling effect of the foam. Flow rates from 0 to 1 mL min^{-1} (inlet temperature: 35 °C) were used and transient temperature changes were outputted to compare with experimental results. The properties of water (default in Fluent) used in the simulations were $\nu_{water} = 0.001$ kg m^{-3} s^{-1} (viscosity), $k_{water} = 0.6$ W m^{-1} K^{-1} (thermal conductivity) and $\alpha_{water} = 0.14$ mm^2 s^{-1} (thermal diffusivity). The solid material properties were $k_{phantom} = 0.42$ W m^{-1} K^{-1} and $\alpha_{phantom} = 0.18$ mm^2 s^{-1} for the skin phantom (Krishnan et al., 2018), $k_{catheter} = 0.22$ W m^{-1} K^{-1} and $\alpha_{catheter} = 0.12$ mm^2 s^{-1} for the skin phantom (Braley, 1970) and $k_{foam} = 0.58$ W m^{-1} K^{-1} and $\alpha_{foam} = 0.14$ mm^2 s^{-1} for the cooling foam (close to the properties of water since it consists ~95% of water).

2.6. Fabricating the thermochromic liquid crystal (TLC) patch

The fabrication process followed established methods (Gao et al., 2014), involving the formation of a thermochromic liquid crystal (TLC) dot array pattern through stamping and transfer using thermal release tape and PDMS with a cylinder array post on a PDMS supporting film. Initially, a thin black PDMS film (~100 μm) was formed by spin-coating and curing a Sylgard 184 mixture (40:1 ratio with curing agent) blended

with 2 wt% iron (II, III) oxide nanopowder (Sigma Aldrich). This film provided an opaque background to facilitate precise colorimetric evaluation of the TLC dots. A PDMS stamp featuring arrays of cylindrical posts (0.5 mm diameters, arranged in a ring shape with an area of approximately ~4.4 cm^2) was pressed onto a layer of chiral nematic liquid crystal slurry (ThermometerSite) applied to a glass slide. Removing the stamp and drying in air yielded a solid layer of TLC material. This stamping and drying process can be iterated multiple times to accumulate sufficient quantity of TLC material on the stamp. A thermal release tape (Nitto, 120 °C) ensured high yield transfer of this TLC solid from the stamp to the surface of the black PDMS film. A transparent thin layer (~200 μm) of PDMS spin-cast onto the black PDMS served as an encapsulation layer. Mounting a cooling foam on the half-cured PDMS layer, followed by complete curing, finalized the fabrication.

2.7. Colorimetric analysis of the TLC dot array skin patch

A Python-based color analysis 453 program (Epicore Biosystems Inc.) employing a standard color calibration card (ColorChecker Classic Nano, Calibrate Inc.) was used to analyze the images captured by a digital camera (EOS 6D, Canon). The transformation of RGB grayscale values to the Commission Internationale de l'Eclairage L*a*b* (CIELAB) color coordinate system established the color space in accordance with the corresponding temperature.

2.8. On-skin measurements

On-skin patient testing began with palpating the VP shunt through the neck or clavicle to identify the location of the superficially positioned shunt. The skin was prepared by cleaning with an alcohol wipe and marking the position of the shunt with a surgical pen. The silicone adhesive (2477P, 3M Inc.) was used to laminate the device. Linear markings on the skin ensured precise alignment of the cooling foam and temperature sensors along the central axis of the shunt over the clavicle (referred to as 'on-shunt'). The device was gently pressed for 5 s to activate the adhesive and laminate it to the skin. For a control, the

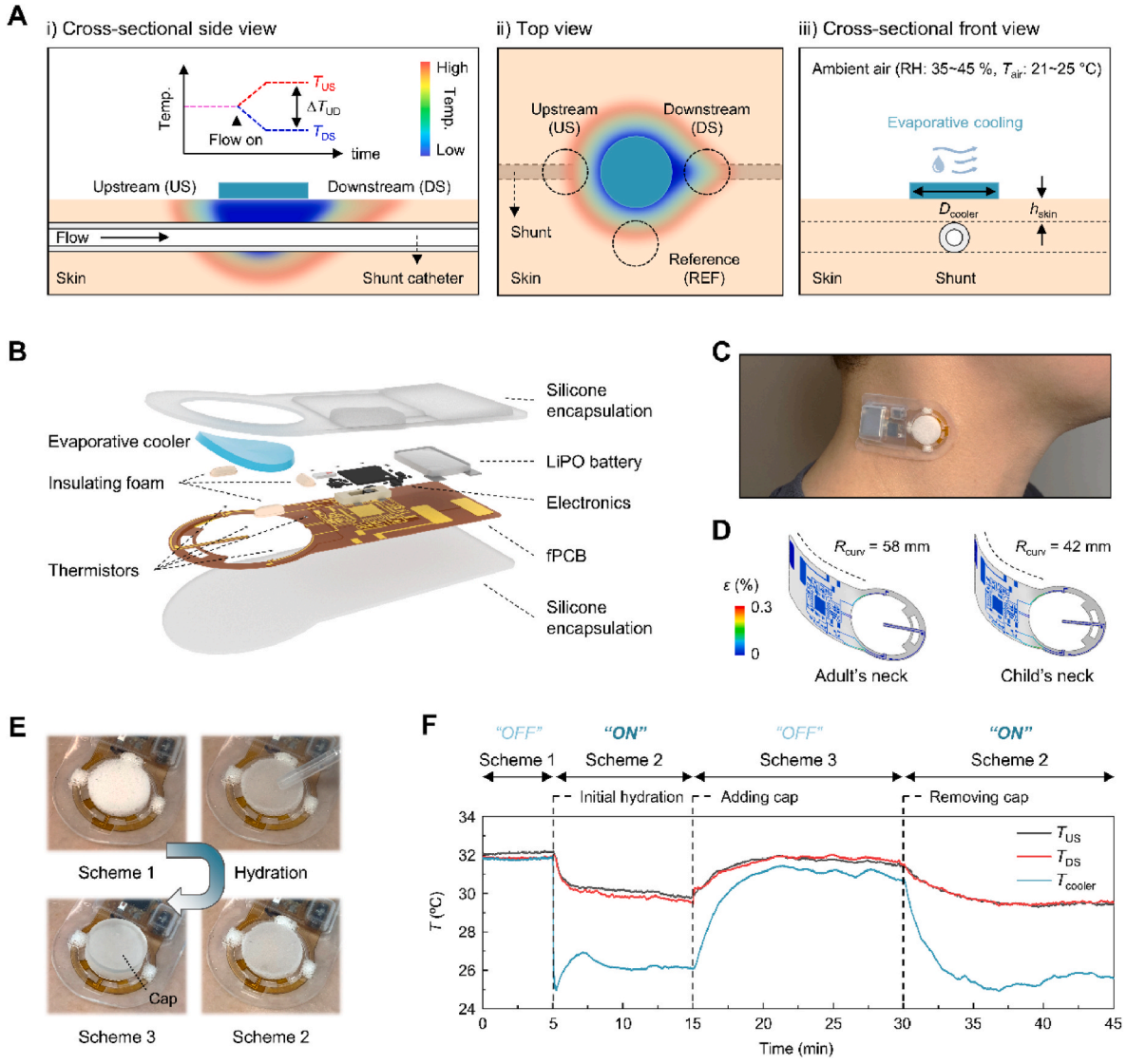

Fig. 1. (A) Low power, evaporative cooling-based wireless sensor for continuous monitoring of flow of cerebrospinal fluid (CSF) through a shunt used to treat hydrocephalus. (B) Exploded view schematic illustration of the device, showing the flexible printed circuit board (fPCB), evaporative cooler, thermally insulating foam, electronic components, and silicone encapsulation layers. (C) Photograph of the device mounted on the skin. (D) Finite element analysis (FEA) of the distributions of strain across the fPCB during bending to a degree comparable to that required to mount on the neck region of a child and adult. (E) Photographs of each step (Fig. 1E, including hydration of the cooling foam) for operating the evaporative cooling mechanism in a switching mode (on and off). (F) Temperature of upstream (T_{US}), downstream (T_{DS}), and cooler (T_{cooler}) regions as a function of time.

device was laminated onto a healthy normal subject at a typical shunt location but away from near-surface vasculature (referred to as 'off-shunt'). Room-temperature water was introduced into the cooling foam using a 1-mL syringe. After ~120 s of full hydration, a temperature drops of approximately −1.0 K from three temperature sensors (located at upstream, downstream, and reference) served as an indication of good contact. Data collection began once the cooling foam is fully hydrated. During measurements, in-hospital patients sat upright (~90° reclining angle). The experimental protocols were approved by the Institutional Review Board of Dankook University (IRB, 2024-12-008). All participants provided their consent before the tests.

3. Results

3.1. Concept illustration

The device introduced here follows well-established principles associated with flow monitoring (Krishnan et al., 2018, 2020) but utilizes a passive cooler based on water evaporation instead of an electrically powered heating element. Specifically, a foam structure saturated with water (Fang et al., 2018) provides a soft, lightweight platform for cooling that can be easily attached/detached from the skin or from a skin-integrated device. A hydrophilic melamine foam is attractive for this purpose due to its ability to adhere robustly to silicone-based elastomers that serve as encapsulation materials for the other components of the device (Fig. S1, Supporting Text 1). The results of detailed characterizations, including morphology and elemental analysis, are presented in Figs. S2–5.

Fig. 1 illustrates a conceptual framework for the study. Positioning the cooler on the surface of the skin above the location of a shunt, the direction, and the rate of flow of CSF leads to distributions of temperature that can be quantitatively interpreted to determine essential flow characteristics. As expected intuitively, the cooler reduces the temperature of the CSF, such that this cooled CSF leads to decreases in temperature at regions along the shunt in the downstream direction (T_{DS}). Similarly, the temperature increases in the upstream region (T_{US}) as the flow of CSF brings thermal power from distant locations to those adjacent to the cooler. The result is a positive temperature difference ($\Delta T_{UD} = T_{US} - T_{DS}$), as a key parameter related to flow (Fig. 1A–i). Measurements of temperature focus on three specific regions (US, DS, and REF; reference), each at an equal distance from the center of the cooler. The two for upstream and downstream align to the shunt and reside at either side of the cooler. The third serves as a reference, largely unaffected by flow (Fig. 1A–ii). As evaporative cooling depends on ambient conditions, such as relative humidity, temperature and wind speed, the most reliable results follow from measurements free of convective effects, in indoor environments at room-temperature. Other important considerations are the diameter of the cooler (D_{cooler}) and thickness of tissue (h_{skin}) between the surface of the skin and the top surface of the shunt (Fig. 1A–iii).

An exploded view schematic illustration in Fig. 1B shows a wireless electronics system that uses these principles for continuous measurements of the flow of CSF through shunts for patients with hydrocephalus. The device consists of a fPCB, an evaporative cooler, thermistors as temperature sensors, various electronic components including a BLE-SoC, a lithium polymer (LiPO) battery, insulating foam, and silicone encapsulation layers. The photograph in Fig. 1C shows the device mounted on the neck of a user. Finite element analysis (FEA) quantifies the mechanical compliance of the device as mounted in this location on an adult (left) and pediatric (right) subject (Fig. 1D). The maximum strain in the functional materials is below 1.5% under bending radii of ~27 mm, and ~37 mm, characteristic for children (Katz et al., 2014) and adults (Kumar et al., 2014), respectively. Four thermistors surround the cooler; one each at the upstream, downstream, and reference locations. The fourth locates at the center between the bottom encapsulation layer and the cooler to measure the temperature of the cooler (T_{cooler}), which is also influenced by flow. Details regarding the characterization of skin temperature during evaporative cooling appear in the Supporting Information (Figs. S6 and S7, Supporting Text 2).

The cooling mechanism can be inactivated or activated by applying or removing a covering, respectively (Fig. S8, Supporting Text 3). Fig. 1E presents a digital photograph of a device attached to the skin in its unhydrated state (Fig. 1E, upper left), uncovered hydrated state (Fig. 1E, lower right) and in this hydrated state covered by a plastic cap (Fig. 1E, lower left). Time dependent measurements of temperature at three locations (T_{US}, T_{DS}, and T_{cooler}) characterize each scheme, the latter two defined as "ON" or "OFF" states (Fig. 1F). Initial hydration after an equilibration period of 5 min activates cooling to place the device in its "ON" state (Fig. 1E, lower right), capable of sensing flow while T_{cooler} remains at ~26 °C. The addition of a cap at 15 min inhibits water evaporation (Fig. S8C), causing all three temperatures to rise to values close to the initial skin temperature (~32 °C) due to inactivation of the cooling process. The device is thus in its "OFF" state (Fig. 1E, lower left), and flow sensing is no longer possible. Removing the cap at 30 min, reactivates evaporative cooling, thereby lowering T_{cooler} back to ~26 °C, and switching the device to its "ON" state (Fig. 1E, lower right). These results highlight that even with a passive cooling mechanism, the flow sensing capabilities in the electronic device can be switched on and off simply by obstructing or enabling evaporative cooling.

3.2. Thermal characterization of the evaporative cooling-based flow sensing system

Benchtop studies and computational modeling efforts facilitate optimization of design parameters (see Methods, Figs. S9–12, and Supporting Text 4 for details). An illustration and digital photograph show the experimental setup (Fig. 2A and B).

Studies of the influence of flow on the evaporative cooling performance involve measurements of T_{cooler}. Measurements use a phantom shunt assembly that includes a catheter (1.3 mm ID/2.5 mm OD) embedded in PDMS at a depth h_{skin} of 0.5 mm. The thermal conductivity and the thermal diffusivity of phantom are 0.42 W m^{-1} K^{-1}, and 0.18 mm^2 s^{-1} (Krishnan et al., 2018), and those of catheter are 0.22 W m^{-1} K^{-1}, and 0.12 mm^2 s^{-1}, respectively (Braley, 1970). Fig. 2C shows measured and computed values as a function of time after initiating flow at rates of 0, 0.05, 0.2, 0.5 and 1.0 mL min^{-1}, respectively. From 0 to 0.05 mL min^{-1}, the change in T_{cooler} is less than 0.15 °C. Significant increases occur above flow rates of 0.2 mL min^{-1}, to values of 1.1, 1.6 and 2.4 °C at flow rates of 0.2, 0.5 and 1.0 mL min^{-1}, respectively, after 3 min. This result indicates that heat transfer associated with the flow of artificial CSF from the upstream direction (~35 °C) to the skin exceeds the heat loss associated with the cooler. Results of FEA with a cooling power of 210 kW m^{-3} are consistent with these experimental results. The thermal effects of flow on the cooler at its interface with the skin exceed those at the exposed upper surface of the cooler, where water evaporation occurs (Fig. S13).

The IR image in Fig. 2D provides a top-view of the phantom shunt assembly, highlighting regions designated for spatially averaged temperature measurement. The upstream (T_{US}), downstream (T_{DS}), and reference (T_{REF}) regions on the skin phantom each have an area of 3.5 mm^2 (diameter: 2.1 mm), and the distance between the center of each region and the center of the cooler is 8.7 mm. Comparisons involve temperature values determined by averaging IR measurements and FEA results across each of these areas, as shown in Fig. 2E, F, at times of 23 s (Fig. 2E), and 120 s (Fig. 2F) after initiating flow at rates of 0, 0.02, 0.05, 0.1, 0.2, 0.3, 0.5, and 1.0 mL min^{-1}. Practical analysis of flow rates focuses on temperatures collected at a characteristic time after initiation of flow. The temperature difference ($T_{US} - T_{DS}$) reaches approximately 63.7% and 95% of its quasi-steady state value (Krishnan et al., 2018, 2020) at ~23 s and ~54 s, respectively. The difference is unchanged, to within experimental uncertainties, after 120 s. T_{US} gradually increases with flow rate, whereas T_{DS} decreases from 0 to 0.1 mL min^{-1} and

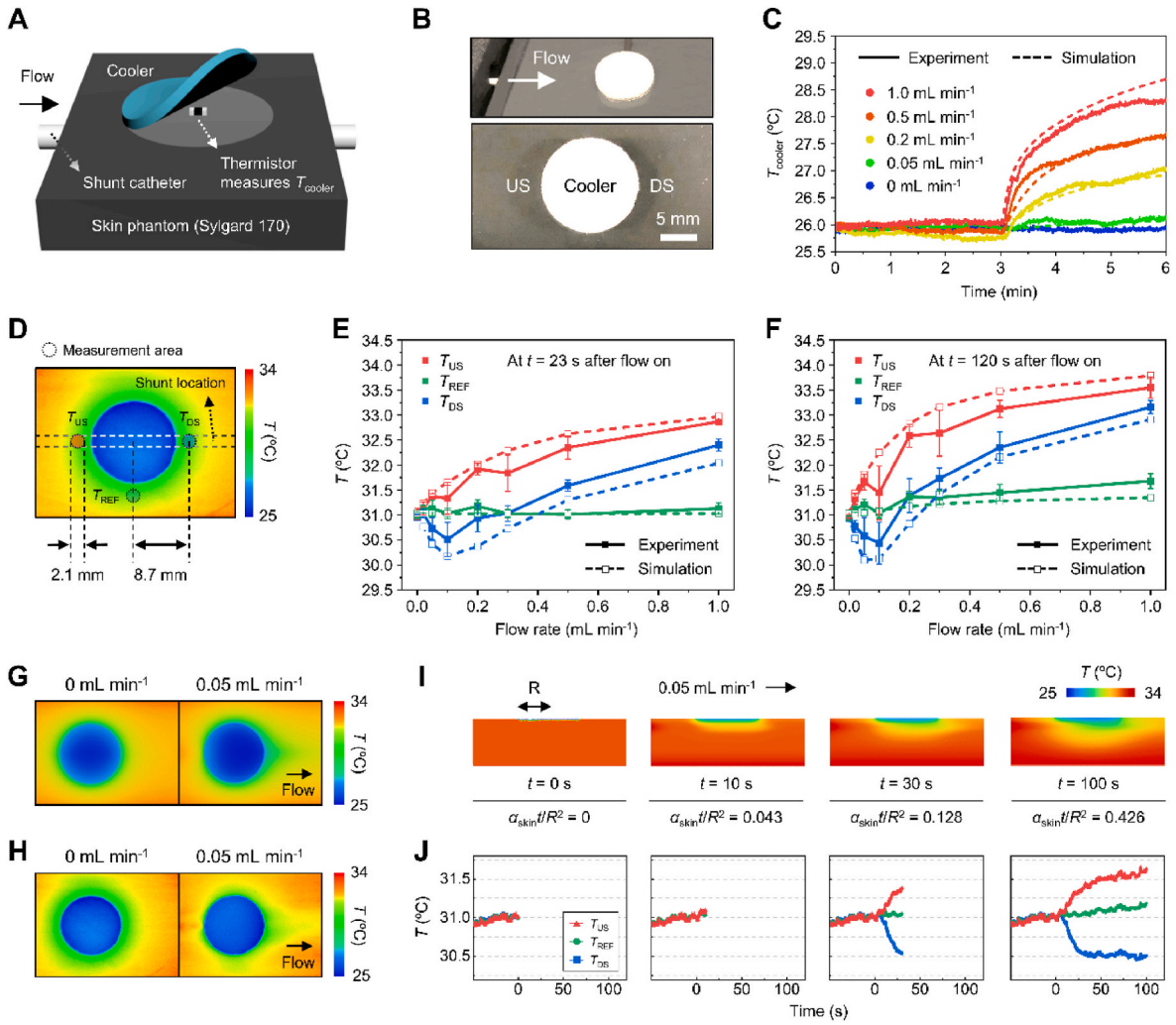

Fig. 2. Thermal characterization of the cooling-based flow sensing mechanism on a phantom shunt assembly. (A) Schematic illustration of the assembly for measurement of the temperature of the cooler (T_{cooler}) using a thermistor. (B) Photograph of the assembly. (C) Experimental and simulation results for T_{cooler}. (D) An IR image displaying locations of the measurement areas and the shunt. (E, F) Experimental and simulation results for T_{US}, T_{DS}, and T_{REF} at 23 s (E) and 120 s (F) after initiating flow (Q = 0.05 mL min^{-1}). (G) Top view of the results of finite element analysis (FEA) showing the effect of cooling in the absence (left) and presence (right) of flow (Q = 0.05 mL min^{-1}). (H) Infrared (IR) images of the evaporative cooler in the absence (left) and presence (right) of flow (Q = 0.05 mL min^{-1}). (I) Cross-sectional view of 3D FEA results illustrating thermal transport through the skin for Q = 0.05 mL min^{-1}. (J) Measured temperatures (T_{US}, T_{REF}, T_{DS}) as a function of time.

subsequently increases again from 0.2 to 1.0 mL min^{-1}. The result is a non-monotonic behavior of $T_{US} - T_{DS}$ with flow rate, consistent with related studies based on the heater-based TPS method (Krishnan et al., 2018, 2020). The values of $T_{US} - T_{DS}$ at 23 s (Fig. 2E) are smaller than those at 120 s (Fig. 2F) across all flow rates, which is reasonable since the values at 120 s are closer to the steady-state conditions. The T_{REF} remains almost constant for all flow rates at both 23 s and 120 s, as expected (Fig. 2E, F). The FEA results in Fig. 2E, F for three temperature values support the experimental data.

FEA results (Fig. 2G) and top-view IR images (Fig. 2H) present temperature distributions in the absence (left panel) and presence (right panel) of flow (Q = 0.05 mL min^{-1}). The cross-sectional representation of the FEA results in Fig. 2I provides additional insights, specifically on the depth sensitivity of the measurement. Further analysis reveals scaling trends in the form of dimensionless quantities based on geometrical parameters and thermal properties of the skin, such as the thermal conductivity (k_{skin}), diffusivity (α_{skin}), thickness (h_{skin}), volumetric flow rate (Q), radius of the cooler (R), and others (Webb et al., 2015). Fig. 2J shows the evolution of temperature for three regions (T_{US}, T_{REF}, T_{DS}) in the presence of flow (Q = 0.05 mL min^{-1}). Before initiating flow (t < 0 s), all three temperatures are ~31 °C. At t = 10 s, these temperatures remain at ~31 °C due to time delays associated with thermal transport. At t = 30 s, T_{US} has increased, T_{DS} has decreased, and T_{REF} has remained approximately the same. The temperature increases of T_{US} result from the flow of warm fluid (~35 °C), while the temperature decreases of T_{DS} result from thermal transport to the cooler. Between 30 and 100 s, the rate of temperature change ($d\Delta T/dt$) gradually decreases and eventually reaches a steady state.

3.3. Benchtop studies using a wireless, continuous flow monitoring device

Integrating a cooling foam with wireless electronics and temperature sensors yields a digital flow sensor with good sensitivity for parameters typical of hydrocephalus patients with shunts that pass through the neck/clavicle region at a depth of 0.5–4.0 mm beneath the skin. The sensitivity decreases sharply for depths greater than ~4 mm, due partly to the relatively long times required for thermal equilibrium between the skin surface and the shunt (Carslaw and Jaeger, 1959; Krishnan et al., 2018). Fig. 3A displays a top view of a device that incorporates a cooling foam, a pair of upstream and downstream NTC thermistors

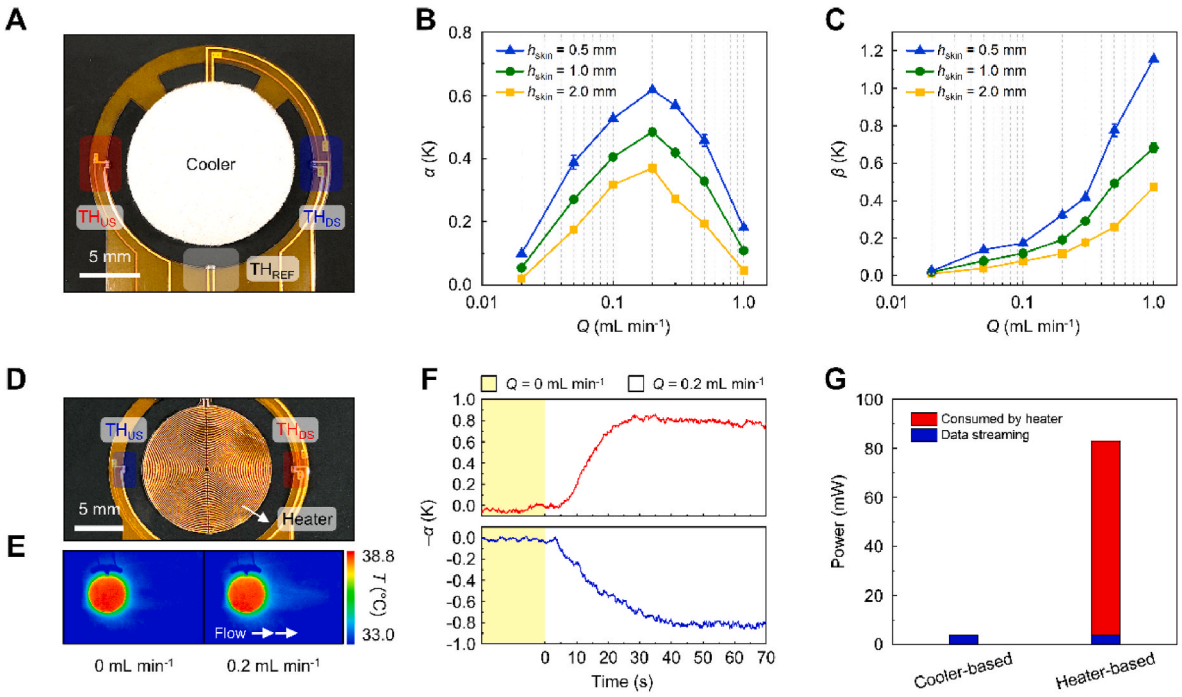

Fig. 3. Power-efficient flow sensing on a phantom shunt assembly. (A) Photograph of the circular cooling foam and sensing elements (thermistors, at upstream (TH_{US}), reference (TH_{REF}), and downstream (TH_{DS}) locations) on a fPCB placed on the skin phantom. (B) Plot of α ($= T_{US} - T_{DS}$) as a function of different physiologically relevant flow rates of a VP shunt ($0.02 \leq Q \leq 1$ mL min^{-1}) and skin thicknesses (h_{skin} = 0.5, 1.0, and 2.0 mm). The results highlight non-monotonic behavior with an inflection point at Q = 0.2 mL min^{-1}. (C) Plot of β ($= T_{US} - T_{REF}$) calculated for the same flow rates and skin thicknesses as in (B). (D, E) Photograph (D) and IR images (E) of the circular heater-based configuration using the same sensing scheme as in (A). (F) Plot of α as a function of time for experiments using the heater (top) and cooler (bottom) as the flow rate changes from Q = 0 to 0.2 mL min^{-1}. (G) Comparison of overall electrical power consumed in cooler- and heater-based devices to induce an equivalent level of average α value (~0.74 K) and to transmit the results to a smartphone via Bluetooth communication.

aligned with the flow direction, and a reference NTC thermistor positioned equidistant from the two thermistors (more details appear in Fig. S14). Thermistors positioned in the upstream, downstream, and reference areas are denoted TH_{US}, TH_{DS}, and TH_{REF} respectively, for recording T_{US}, T_{DS}, and T_{REF}, respectively (Fig. 3A, D). A useful parameter, α, defined as ($T_{US} - T_{DS}$) serves to quantify the flow-induced thermal anisotropy. T_{US} and T_{DS} represent the changes in temperature from a steady-state baseline after a thermal equilibration time of ~5 min after initiating cooling (Fig. 1E). For a phantom shunt assembly with a catheter (1.3 mm ID/2.5 mm OD) embedded in phantom with h_{skin} of 0.5 mm, α increases from ~0 K to a positive value when the flow changes stepwise from 0 to 0.2 mL min^{-1} (Fig. 3B). The flow initiates at time t = 0 s, resulting in a transient temperature rise that can be fit to the form

$$\frac{\alpha(t)}{\alpha_{qss}} = \alpha_0 + Ae^{R_0 t}$$

where α_{qss} is a quasi-steady state value of α such that

$$\left(\frac{\partial \alpha(t)}{\partial t}\right)_{\alpha=\alpha_{qss}} \approx 0$$

with α_0, A, and R_0 are 0.97, −1.02, and −0.05, respectively (Fig. S15). Analysis indicates that $\alpha(t)$ attains ~63.7% of its quasi-steady state value at t = 22.6 s, after initiation of flow. The temperature then reaches ~95% of its steady-state value after ~54 s. These behaviors are consistent with those obtained by IR imaging, as expected. The transient change in α in response to a change in flow follows from thermal transport through the underlying skin to the shunt, with additional dependence on the thermal mass of the thermistors, and the constituent materials (copper and polyimide) of the fPCB.

Fig. 3B shows the dependence of α on flow rate across a physiologically relevant range for CSF in shunted hydrocephalus patients ($0.02 \leq Q \leq 1$ mL min^{-1}) (Brendel et al., 1983; Chervu et al., 1984; Drake et al., 1991; Kadowaki et al., 1995) at three different skin thicknesses (h_{skin} = 0.5, 1.0, and 2.0 mm). As supported by the results in Fig. 2E, α exhibits non-monotonic changes with flow rate, similar to behaviors observed using heater-based systems (Krishnan et al., 2018, 2020; Webb et al., 2015), but the position of the peak sensitivity ($\alpha \approx 0.62$ K) appears at 0.2 mL min^{-1}. To discriminate between flow rates that have identical values of α on either side of the peak value, a second parameter, $\beta \equiv (T_{US} - T_{REF})$, can be considered. The T_{REF} serves as a good basis as it is measured by TH_{REF} located at the same distance as the other two thermistors from the center of the cooling foam. T_{DS} varies non-monotonically with flow rate, decreasing with flow for $0.02 \leq Q \leq 0.1$ mL min^{-1} and increasing with flow for $Q \geq 0.1$ mL min^{-1}. In contrast, both T_{US} and T_{REF} exhibit an increasing trend with flow for the entire range of flow rates, but the magnitude of the increase in T_{US} is greater than that in T_{REF} (Fig. 2E). As a result, β increases monotonically with flow for all skin thicknesses, to yield important information about the flow regime (i.e., low flow vs. high flow) (Fig. 3C). Furthermore, compared to α, monitoring β improves the sensitivity in measurements of flow at high flow rates. Results of analysis of variance (ANOVA) with F-test confirm the reliability of the device for flow measurements (Table S1, Supporting Text 5).

Benchtop studies with this phantom shunt assembly allow for comparisons of the performance of the evaporative cooling-based and a Joule heater-based device, both with the same geometries and layouts. The measurements use heating powers that induce α values similar to those achieved with the cooling foam. Fig. 3D shows a top view of the device that uses a heater, with a pair of TH_{US} and TH_{DS} aligned with the flow direction. The IR image in Fig. 3E displays thermal distributions in the absence (left panel) and presence (right panel) of flow (Q = 0.2 mL min^{-1}) during heating. Fig. 3F depicts the change in $-\alpha$ ($= T_{DS} - T_{US}$) for the two cases (upper: using a heater, bottom: using a cooler) when the

flow rate changes stepwise from 0 to 0.2 mL min^{-1}. With the heater (cooler), $-\alpha$ becomes positive (negative) as the flow absorbs (releases) heat while passing beneath the heater (cooler). With flow ($Q = 0.2$ mL min^{-1}), $-\alpha$ changes after a few seconds of delay, subsequently stabilizing at a constant value (~0.8 K and ~−0.8 K for the heater and cooler cases, respectively). The cooler requires zero power whereas the heater consumes ~79 mW. As a result, the device based on evaporative cooling consumes only ~4 mW, to enable the wireless electronics; the one based on Joule heating requires a total of ~83 mW, dominated by the heater (Fig. 3G). This factor of 20 advantage in power consumption has practical consequences in the lifetime of the battery and, thus, the number of cycles of use that can be supported. The controllability of evaporative cooling, along with the effects of ambient air temperature and skin temperature on evaporative cooling performance in the flow sensing device, is also systematically confirmed (Figs. S16–19, Supporting Text 6 and 7). Another key advantage of evaporative cooling is that it eliminates any potential risk for pain or thermal injury to the skin (Rolke et al., 2006; Spray, 1986).

3.4. On-skin sensing of CSF flow

Pilot tests with shunt recipients in indoor environments verify the feasibility of clinical monitoring using this evaporative cooling-based method for flow sensing. A controlled test environment with minimal patient movement limits air convection, thus allowing for uniform, consistent levels of evaporative cooling. The flow sensing device used in this study is designed to be compact, lightweight, and energy-efficient, making it well-suited to support pilot tests (Fig. S20, Supporting Text 8 and 9). Successive measurements involve placement of device on the skin over the distal catheter (Fig. 4A, Fig. S21). Linear markings on the

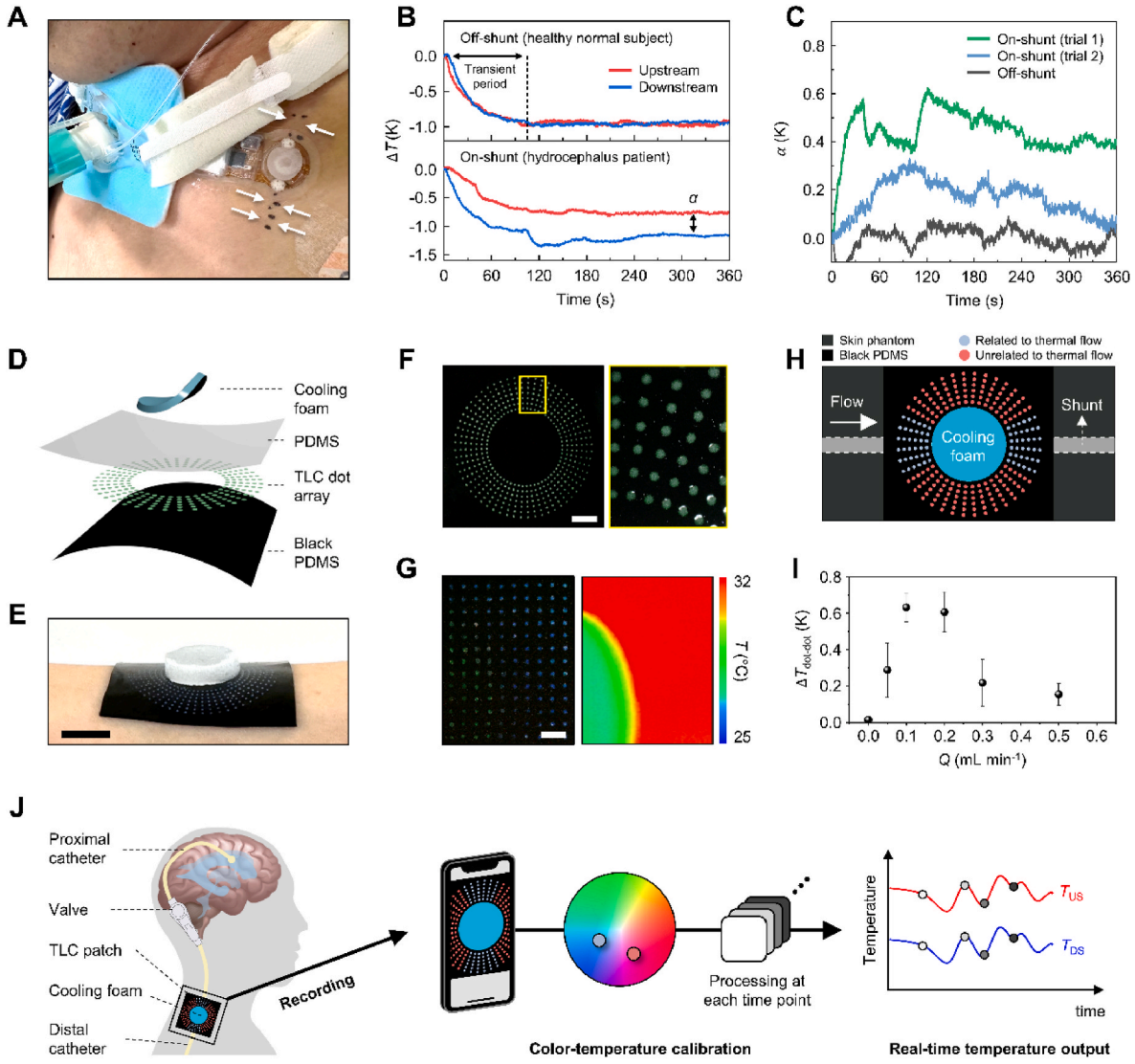

Fig. 4. (A) Photograph of device mounted on skin over shunt. Participants provided written informed consent for their photos/images to be included as a part of this publication. (B) Temperatures measured from upstream and downstream sensors during off-shunt measurements at the base of the pectoral muscle distal to the clavicle in a healthy normal subject (top), and during on-shunt measurements at the shunt location in a hydrocephalus patient (bottom). (C) Plot of α computed for two separate trials on the same patient over the shunt, and one trial at an off-shunt location on the healthy normal subject. (D) An exploded view illustration of the thermochromic liquid crystal (TLC) dot array skin patch for flow sensing without integrated electronics. (E, F) Digital images of the TLC patch mounted on the forearm (E), and a top view of the TLC patch without the cooler (F). The scale bar is 10 mm in (E) and 5 mm in (F), respectively. (G) Digital (left) and IR (right) images of a TLC patch consisting of a 10 × 13 array of pixels, captured on a hot plate with an area that is partially cooled. The scale bar is 2 mm. (H) An illustration of a TLC patch mounted on a phantom shunt assembly. Light blue dots indicate areas that can be highly affected by flow. (I) Plot of $\Delta T_{dot\text{-}dot}$ at the flow rates of 0, 0.05, 0.1, 0.2, 0.3, and 0.5 mL min^{-1}. (J) Application concepts of the TLC patch for flow sensing. (For interpretation of the references to color in this figure legend, the reader is referred to the Web version of this article.)

skin facilitate the precise alignment of the central axis of the cooling foam and temperature sensors along the underlying shunt over the clavicle (referred to as 'on-shunt'). Measurements on a healthy normal subject at a typical shunt location, but away from near-surface vasculature (Fig. 1C), serves as a control to represent the 'off-shunt' condition.

The presence or absence of flow, indicating shunt functioning or failure, can be determined by observing the presence or absence of thermal anisotropy. In the absence of flow, or at an appropriate 'off-shunt' location, activating the cooling (i.e. fully hydrating the foam) immediately results in a local temperature drop (~1 K) at both the upstream and downstream temperature sensors positioned 8.7 mm away from the center of the cooling foam (Fig. 4B, upper panel), consistent with the results from the benchtop setup (Fig. 2G, H, and Fig. S12). After the transient period (~105 s), the temperature values reach equilibrium, indicating that the thermal response due to the cooling foam is complete and no additional factors contribute to thermal anisotropy between the upstream and downstream sensors. The measured values of T_{cooler} from the on-skin measurements are in Fig. S22. Calculations of α values from the measured temperatures focus only on the quasi-steady state response, defined as the operational phase following the transient period (Krishnan et al., 2018, 2020). In the presence of flow, or at the appropriate 'on-shunt' location, similar measurements reveal clear thermal anisotropy. Here, changes in temperature follow a trend (Fig. 4B, lower panel) that is different compared to the 'off-shunt' case, as expected in the collective results in Fig. 2. On-shunt measurements averaged over 250 s after the transient 105 s period yield root-mean-square (RMS) values of alpha (α_{RMS}) of ~0.51 K in trial 1 and ~0.18 K in trial 2. Off-shunt measurements show α_{RMS} values of 0.03 K, with a standard deviation of 0.04 K, resulting in signal-to-noise ratio (SNR) values of ~28 in trial 1, and ~10 in trial 2 (Fig. 4C, Table S2). These results indicate that very low flow rates, characterized by a measured α values of ~0.15 K or less, reach the limits of detection of this system. Upon reliable measurement of α values, the absolute value of the flow rate can be determined by modeling with key parameters, including the thermal transport properties of the skin and the shunt, along with its depth and geometrical features.

3.5. Colorimetric analysis of flow using thermochromic liquid crystal (TLC) dot array skin patch

Further reductions in power requirements and costs follow from the use of colorimetric mechanisms for measurements of temperature, as alternatives to electronic schemes. TLC materials transition through various phases from solid crystals to smectic, cholesteric, and ultimately isotropic liquid with increasing temperature (Dolphin et al., 1973; Phillip, 2018). Colorimetric analysis exploits temperature dependent shifts in the peak wavelengths of the reflected light from pixelated regions of TLC. A skin-integrated patch that incorporates TLC dot arrays (Gao et al., 2014) and mechanisms for evaporative cooling can exploit the principles described previously for measuring flow through analysis of digital images of the device structure during operation.

Fig. 4D presents an exploded view illustration of such a patch incorporating TLC dot array and a cooling foam. A thin film of PDMS serves as the soft substrate above and below the array of TLC dots, each with a diameter of ~0.5 mm (see Methods). Designs consider the analysis of spatially averaged temperature measurements of the skin phantom around the cooling foam as presented in Fig. 2. A digital image in Fig. 4E depicts the soft, flexible TLC skin patch conformally attached on the forearm. Fig. 4F shows a top view of the patch without the cooling foam, and an enlarged view of the TLC dot array highlighted by the yellow square. The chiral nematic liquid crystal slurry offers a dynamic range of 24–30 °C (Fig. S23) for colorimetric temperature analysis, well matched to the application explored here, given that the cooling foam reduces the skin temperature to ~26 °C (Fig. 1E). Fig. 4G shows a digital (left), and IR (right) image for a TLC patch consisting of a 10 × 13 array of pixels, captured on a hot plate that has a partially cooled area. The change in color of the TLC dot array appears within a few seconds upon exposure to surfaces with distinct temperatures. The CIE color space ($L^*a^*b^*$) of a single TLC dot, corresponding to its temperature, can be extracted using computer vision technology through light-corrected data transformation from a digital image (Figs. S23A and B). A linear calibration curve connecting the chromatic b^* value with temperature enables the TLC dots to be utilized as a collection of temperature sensors (Fig. S23C).

Demonstrations of colorimetric detection of flow utilize the phantom shunt assembly described previously (Fig. 4H and Fig. S24A). In the TLC dot arrays on the skin patch mounted on the phantom shunt assembly, blue-highlighted areas indicate the upstream and downstream regions influenced by thermal flow (Fig. 4H). These dots undergo temperature changes due to flow-induced heat transport, leading to observable color shifts in the TLC dots. In contrast, red-highlighted areas, positioned outside the shunt location, are unaffected by thermal flow. These dots retain their characteristic color, corresponding to a temperature slightly below the temperature of the skin due to the cooling foam, without any color shift in the TLC dots. Spatially averaged temperatures of each region can be determined through color-to-temperature transformations (Fig. 4I). A digital camera yields top-view images of the system under two conditions: in the absence of flow, and 120 s after initiating flow. Image processing focuses on four dots near both the upstream and downstream regions using a Python-based color analysis program (Fig. S24B). $\Delta T_{dot\text{-}dot}$ represents the difference in spatially averaged temperatures between the upstream and downstream regions, measured from the TLC dot array. These values follow from color-to-temperature transformations applied to the four dots located each in the upstream and downstream regions. Fig. 4I presents a plot of $\Delta T_{dot\text{-}dot}$, showing measured values of 0.02 K (± 0.02 K), 0.29 K (± 0.15 K), 0.63 K (± 0.08 K), 0.61 K (± 0.11 K), 0.22 K (± 0.13 K), and 0.15 K (± 0.06 K) at flow rates of 0, 0.05, 0.1, 0.2, 0.3, and 0.5 mL min^{-1}, respectively.

4. Discussion and conclusion

This study introduces an advanced version of our previously published platforms (Krishnan et al., 2020), designed to enable continuous, low-cost, wireless on-skin measurements of CSF flow in shunts by thermal mechanisms that involve cooling through simple water evaporation. This type of device offers significant potential for the indoor treatment and care of patients with hydrocephalus for clinical diagnostics in an energy-efficient manner that reduces the bill of materials for analogous devices that rely on heating. The colorimetric flow sensing scheme, utilizing a TLC patch, promises significant further reductions in energy consumption, device costs, and design complexity. Future work will focus on further enhancements to improve measurement accuracy, such as: (i) enhancing evaporative cooling power, (ii) improving the spatial and temperature resolution of the TLC platform, and (iii) developing advanced image processing technologies compatible with standard smartphones to enable flow measurements through simple image capture or video recording, subsequent autonomous color-temperature calibration (Fig. 4J). Finally, the approaches reported here can be applied not only to measurements of CSF flow but to assessments of flow of various biofluids, such as sweat (Kwon et al., 2021) and macrovascular blood (Webb et al., 2015), thereby enhancing their applicability for a wide range of medical conditions and diagnostic purposes.

CRediT authorship contribution statement

Minsu Park: Writing – review & editing, Writing – original draft, Visualization, Validation, Methodology, Investigation, Data curation, Conceptualization. **Shupeng Li:** Writing – review & editing, Data curation. **Kyeong Min Song:** Validation, Methodology, Data curation. **Kyeongha Kwon:** Software, Methodology. **Jung-Ho Yun:** Methodology, Investigation. **Raudel Avila:** Methodology. **R. Chad Webb:**

Writing – review & editing, Methodology. **Hany M. Arafa:** Methodology. **Soongwon Cho:** Methodology. **Geumbee Lee:** Methodology. **Chase Correira:** Methodology. **Bosung Kim:** Methodology. **Yu Bin Kim:** Methodology. **Hyoun Ji Ha:** Methodology. **Woo-Youl Maeng:** Methodology. **Jae-Young Yoo:** Investigation. **Hyoyoung Jeong:** Investigation. **Hanjun Ryu:** Methodology. **Sang Min Won:** Methodology. **Yei Hwan Jung:** Methodology. **Yoonseok Park:** Methodology. **Seong Jun Kang:** Writing – review & editing, Resources. **Yonggang Huang:** Writing – review & editing, Validation, Software. **John A. Rogers:** Writing – review & editing, Writing – original draft, Supervision.

Declaration of competing interest

The authors declare the following financial interests/personal relationships which may be considered as potential competing interests: John A. Rogers is a co-founder of Rhaeos, a company focused on developing and commercializing noninvasive, wireless, wearable flow sensors for assessing cerebrospinal fluid flow.

Acknowledgments

This work was supported by the Querrey-Simpson Institute for Bioelectronics. This work made use of the NUFAB facility of Northwestern University's NUANCE Center, which has received support from the SHyNE Resource (NSF ECCS-2025633), the IIN, and Northwestern's MRSEC program (NSF DMR-2308691). The present research was supported by the research fund of Dankook University in 2025.

Appendix. ASupplementary data

Supplementary data to this article can be found online at https://doi.org/10.1016/j.bios.2025.117349.

Data availability

Data will be made available on request.

References

Al-Tamimi, Y.Z., Sinha, P., Chumas, P.D., Crimmins, D., Drake, J., Kestle, J., Hayward, R., Solanki, G.A., Thomson, S., Thorne, J., 2014. Neurosurgery 74, 29.
Bork, T., Hogg, A., Lempen, M., Müller, D., Joss, D., Bardyn, T., Büchler, P., Keppner, H., Braun, S., Tardy, Y., Burger, J., 2010. Biomed. Microdevice 12, 607.
Braley, S., 1970. J. Macromol. Sci., Chem. 4, 529.
Brendel, A.J., Wynchank, S., Castel, J.P., Barat, J.L., Leccia, F., Ducassou, D., 1983. Radiology 149, 815.
Carslaw, H.S., Jaeger, J.C., 1959. Clarendon Press, 2nd Ed.
Chervu, S., Chervu, L.R., Vallabhajosyula, B., Milstein, D.M., Shapiro, K.M., Shulman, K., Blaufox, M.D., 1984. J. Nucl. Med. 25, 91.
Chiba, Y., Yuda, K., 1980. J. Neurosurgery (Baltim.) 52, 700.
Dolphin, D., Muljiani, Z., Cheng, J., Meyer, R.B., 1973. J. Chem. Phys. 58, 413.
Drake, J., Sainte-Rose, C., DaSilva, M., Hirsch, J.-.F., 1991. Neurosurgery 28, 242.
Fang, Z., Jiao, S., Wang, B., Yin, W., Pang, G., 2018. Global Challenges 3, 1800085.
Gao, L., Zhang, Y., Malyarchuk, V., Jia, L., Jang, K.-I., Webb, R.C., Fu, H., Shi, Y., Zhou, G., Shi, L., Shah, D., Huang, X., Xu, B., Yu, C., Huang, Y., Roger, J.A., 2014. Nat. Commun. 5, 4938.
Gok, B., Batra, S., Eslamy, H., Rigamonti, D., Ziessman, H., 2013. Clin. Nucl. Med. 38, 527.
Gustafsson, S.E., 1991. Rev. Sci. Instrum. 62, 797.
Ha, J., Borzage, M., Vanstrum, E., Doyle, E., Upreti, M., Tamrazi, B., Nelson, M., Blüml, S., Johal, M., McComb, J., Chu, J., Durham, S., Krieger, M., Moats, R., Chiarelli, P., 2023. J. Neurosurg. 140 (4), 1117–1128.
Kadowaki, C., Hara, M., Numoto, M., Takeuchi, K., Saito, I., 1995. Childs Nerv. Syst. 11, 203.
Kahle, K.T., Kulkarni, A.V., Limbrick, D.D., Warf, B.C., 2016. Lancet 387, 788.
Katz, S., Vaccani, J.-.P., Clarke, J., Hoey, L., Colly, R.C., Barrowman, N.J., 2014. BMC Pediatr. 14, 159.
Kestle, J., Drake, J., Milner, R., Sainte-Rose, C., Cinalli, G., Boop, F., Piatt, J., Haines, S., Schiff, S., Cochrane, D., Steinbok, P., MacNeil, N., 2000. Pediatr. Neurosurg. 33, 230.
Kim, B.J., Jin, W., Baldwin, A., Yu, L., Christian, E., Krieger, M.D., McComb, J.G., Meng, E., 2016. Biomed. Microdevices 18, 87.
Koschnitzky, J.E., Yap, E., Zhang, Y., Chau, M.J., Yerneni, K., Somera, A.L., Luciano, M., Moghekar, A., 2023. J. Neurosurg. 139, 502.
Krishnan, S.R., Arafa, H.M., Kwon, K., Deng, Y., Su, C.-.J., Reeder, J.T., Freudman, J., Stankiewicz, I., Chen, H.-.M., Loza, R., Mims, M., Mims, M., Lee, K., Abecassis, Z., Banks, A., Ostojich, D., Patel, M., Wang, H., Börekçi, K., Rosenow, J., Tate, M., Huang, Y., Alden, T., Potts, M.B., Ayer, A.B., Rogers, J.A., 2020. npj Digit. Med. 3, 29.
Krishnan, S.R., Ray, T.R., Ayer, A.B., Ma, Y., Gutruf, P., Lee, K., Lee, J.Y., Wei, C., Feng, X., Ng, B., Abecassis, Z.A., Murthy, N., Stankiewicz, I., Freudman, J., Stillman, J., Kim, N., Young, G., Goudeseune, C., Ciraldo, J., Tate, M., Huang, Y., Potts, M., Rogers, J.A., 2018. Sci. Transl. Med. 10, eaat8437.
Kumar, N.V., Ismail, M.H., P, M., M, G., Tripathy, M., 2014. J. Clin. Diagn. Res. 8, MC23.
Kwon, K.H., Kim, J.U., Deng, Y., Krishnan, S.R., Choi, J., Jang, H., Lee, K.H., Su, C.-J., Yoo, I., Wu, Y., Lipschultz, L., Kim, J.-H., Chung, T.S., Wu, D., Park, Y., Kim, T-i., Ghaffari, R., Lee, S., Huang, Y., Rogers, J.A., 2021. Nat. Electron. 4, 302.
Linninger, A.A., Xenos, M., Zhu, D.C., Somayaji, M.R., Kondapalli, S., Penn, R.D., 2007. IEEE Trans. Biomed. Eng. 54, 291.
Liptak, G.S., McDonald, J.V., 1985. Pediatr. Neurosurgery (Baltim.) 12, 289.
Madhvapathy, S.R., Arafa, H.M., Patel, M., Winograd, J., Kong, J., Zhu, J., Xu, S., Roger, J.A., 2022. Appl. Phys. Rev. 9, 041307.
Madsen, J., Abazi, G., Fleming, L., Proctor, M., Grondin, R., Magge, S., Casey, P., Anor, T., 2011. Neurosurgery 68, 198.
McGirt, M.J., Leveque, J.-.C., Wellons III, J.C., Villavicencio, A.T., Hopkins, J.S., Fuchs, H.E., George, T.M., 2002. Pediatr. Neurosurgery (Baltim.) 36, 248.
Phillip, H.M., 2018. Encyclopedia of Modern Optics, second ed.) 3, p. 8.
Rolke, R., Baron, R., Maier, C., Tölle, T.R., Treede, R.-D., Beyer, A., Binder, A., Birbaumer, N., Birklein, F., Bötefür, I.C., Braune, S., Flor, H., Huge, V., Klug, R., Landwehrmeyer, G.B., Magerl, W., Maihöfner, C., Rolko, C., Schaub, C., Scherens, A., Sprenger, T., Valet, M., Wasserka, B., 2006. Pain 123, 231.
Spray, D.C., 1986. Annu. Rev. Physiol. 48, 625.
Vassilyadi, M., Tataryn, Z.L., Alkherayf, F., Udjus, K., Ventureyra, E.C.G., 2010. J. Neurosurg. Pediatr. 6, 468.
Webb, R.C., Ma, Y., Krishnan, S., Li, Y., Yoon, S., Guo, X., Feng, X., Shi, Y., Seidel, M., Cho, N.H., Kurniawan, J., Ahad, J., Sheth, N., Kim, J., Taylor VI, J.G., Darlington, T., Chang, K., Huang, W., Ayers, J., Grubele, A., Pielak, R.M., Slepian, M.J., Huang, Y., Gorbach, A.M., Rogers, J.A., 2015. Sci. Adv. 1, e1500701.
Zarrin, D.A., Jafari, M., Kim, W., Colby, G.P., 2023. Front. Bioeng. Biotechnol. 11, 1.